PHYSICAL REVIEW B **111**, 134416 (2025)

Tunable toroidic phase transition in one-dimensional antiferromagnetic ferrotoroidic semiconductor

Jin Zou,[1,2] Wuxuan Li,[2] Yechen Xun,[3] Hua Wang,[4,*] and Jingshan Qi[1,†]
[1]*Tianjin Key Laboratory of Quantum Optics and Intelligent Photonics, School of Science, Tianjin University of Technology, Tianjin 300384, China*
[2]*School of Physics and Electronic Engineering, Jiangsu Normal University, Xuzhou 221116, China*
[3]*Department of Physics and Astronomy, The University of Tennessee, Knoxville, Tennessee 37996, USA*
[4]*Center for Quantum Matter, School of Physics, Zhejiang University, Hangzhou 310058, China*

(Received 20 October 2024; revised 19 February 2025; accepted 24 March 2025; published 10 April 2025)

The antiferromagnetic (AFM) spintronics have aroused comprehensive interest due to the fast magnetic dynamic response and lack of stray fields. However, probing and manipulating AFM order has always been a scientific challenge due to the lack of macroscopic statistical magnetic moments and insensitivity to external fields. So, the discovery, control, and detection of AFM materials has important scientific and practical significance. In this paper, we propose a strategy to control and detect the AFM order through electrical and optical methods, and demonstrate its feasibility with a group of one-dimensional (1D) materials MoX_3(X = Cl, Br, I) as examples. The basic concept is to use the antisymmetric Compton profile to distinguish the ferrotoroidic order and antiferrotoroidic order in the 1D AFM spin chain based on the magnetoelectric multipole theory. MoX_3 is predicted to be an AFM semiconductor by the anisotropic Heisenberg model and Monte Carlo simulation. Moreover, under hole doping the magnetic ground state can switch between two different AFM states with different symmetry and short-range vortex order. More interesting, two different AFM orders, respectively, correspond to 1D ferrotoroidic and antiferrotoroidic states. Due to the existence of toroidal moment in ferrotoroidic state, the Compton scattering provides an intuitive detection of magnetic configurations by optical method. Through symmetry analysis and theoretical calculations, we show that the antisymmetric Compton profile serves as a detectable fingerprint that can be used to distinguish the symmetry-dependent toroidic phase transition or AFM orders. One-dimensional materials have potential application prospect in the development of miniaturization and high-density integration of devices while maintaining 1D electron transport. Therefore, the tunable and detectable AFM order endows 1D MoX_3 chain with great possibility for future applications in AFM spintronics.

DOI: 10.1103/PhysRevB.111.134416

I. INTRODUCTION

Spintronics is an attractive branch of condensed matter physics, which involves the utilization of electronic spin for information storage and processing [1]. Low-dimensional spintronic materials with high spin polarization and high Curie temperature are highly desirable for practical applications [2]. Ferromagnets provide a potential platform for practical devices with noticeable spintronic effects due to the intrinsic magnetic order [3]. This makes it possible to create magnetic random-access memory, which has unique advantages over semiconductor-based alternatives including nonvolatility, extended durability, and low power consumption.

Different from ferromagnets, antiferromagnets have been largely ignored due to their vanishing statistical magnetization and insensitivity to magnetic fields, posing fundamental challenges for probing and manipulating the antiferromagnetic (AFM) order, which only work as passive ingredients in magnetic tunnel junctions by pinning adjacent ferromagnets. However, compared to ferromagnets, AFM materials have ultrahigh dynamic speed and low sensitivity to stray magnetic fields, which makes them more efficient for high-speed device operation. So, AFM spintronic devices have received much attention in recent years [4–6]. But, the two most fundamental functions of the AFM sequence as a data storage device are control and reading, which is a key challenge in AFM spintronics.

In addition, in order to meet the demands of device miniaturization, materials science is undergoing the evolution of dimensionality reduction from 3D to 2D and now to 1D [7]. Recent developments have shown that reducing material dimensions from a single atom sheet to a single atom chain not only opens new avenues for practical applications but also leads to breakthroughs in fundamental theory. Examples include high critical temperature superconductivity in 1D iron or copper chains and ladders [8,9], ferroelectricity induced by phonon modes or spin ordering [8], charge-density wave or spin-density wave states [10], spin block states in the orbital-selective Mott regime of iron 1D ladders or chains [11], and so on. This can, to some extent, compensate for the drawbacks of higher-dimensional materials. Atomic chains not only

---

[*] Contact author: daodaohw@zju.edu.cn
[†] Contact author: qijingshan@email.tjut.edu.cn

offer dimensional advantages but also expand and strengthen the properties of original bulk or high-dimensional materials, facilitating theoretical model development and experimental control of the correlation between various physical properties [12]. One-dimensional magnetic systems, usually in the form of spin chains, have become a thriving field of research, illustrating many key concepts in many-body quantum physics and even inspiring the recent search for new phases of matter, such as the Majorana fermion [13–15]. Recently, many 1D magnetic materials have been investigated by both experimental and theoretical approaches, including 1D $OsCl_4$ [11], $CrSbSe_3$ [16,17], TiI_3 [18], VI_3 [19], $CuBr_3$ [20], and WOI_3 [21]. However, developing efficient and feasible methods to regulate and detect the AFM order in 1D materials remains a huge challenge.

In this work, we have proposed a strategy to control and detect the AFM order through electrical and optical methods, and taken a group of 1D materials MoX_3 (X = Cl, Br, I) as examples to demonstrate the feasibility of strategy. We predicted a stable 1D MoX_3 dimeric chain, characterized by alternating short and long Mo-Mo pairs along the period direction. The magnetic ground state is an AFM semiconductor, with an easy plane perpendicular to the chain direction and a large magnetic anisotropy energy (MAE). Moreover, under hole doping, the magnetic ground state switches between two distinct AFM orders with different symmetry due to a sign change in the exchange interactions between second-nearest neighboring Mo atoms. Interestingly, these two different AFM orders correspond, respectively, to 1D ferrotoroidic and antiferrotoroidic states. Through symmetry analysis and theoretical calculations of antisymmetric Compton profile we elucidate the different responses of two AFM orders and underlying physical mechanism.

II. RESULTS AND DISCUSSION

A. Concept and mechanism

Ferroic materials exhibit spontaneous ordering of spin, charge, or strain. The AFM order is a spin-ordered state, but it lacks a net magnetic dipole, making its measurement a challenging task. Although some methods such as neutron diffraction [22,23] and second-harmonic generation [24,25] have been used for measuring AFM order, new alternative methods still need to be explored for different applications and convenience. There is a special AFM order that can induce the toroidal moments, known as the ferrotoroidic order. It can be described by defining a toroidal moment, $\vec{t}=\sum_i \vec{r}_i\times\vec{s}_i$, where $\vec{r}_i$ and $\vec{s}_i$ are the position and spin vector of the ith ion, respectively, and the sum covers all ion positions in the cell. The intensity of toroidal moment can be defined as the toroidal moment per unit volume, $\vec{T}=\vec{t}/V$. As shown in Fig. 1, the uniform arrangement of 1D AFM spin chain results in a nontoroidal state due to the complete cancellation of adjacent toroidal moment. However, 1D AFM spin chain arranged in dimerization generates a 1D ferrotoroidic state due to the net toroidal moment. Similar to the definition of ferroelectric polarization, the periodicity leads to uncertainty in the value of toroidal moment. Therefore, according to the definition of polarization intensity in periodic systems, the intensity of toroidal moment can be defined as the difference between the ferrotoroidic state and the nontoroidal state [26] and thus it will have a uniquely determined value $\vec{T}=\frac{sd}{4}$, which is an observed physical quantity.

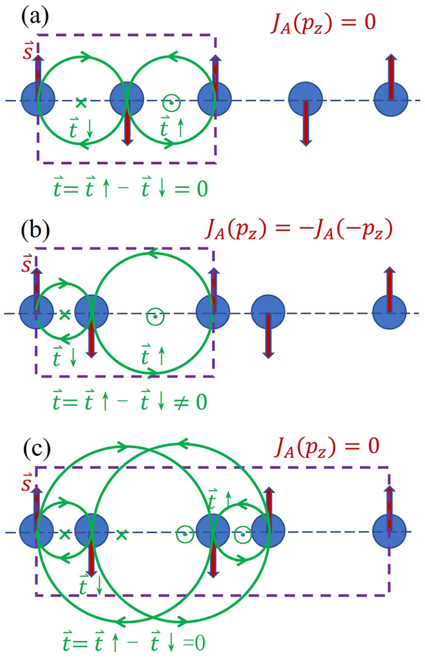

FIG. 1. (a) A uniformly arranged 1D AFM spin chain model with zero toroidal moment. (b) A dimerized 1D AFM spin chain model with a net toroidal moment. (c) A dimerized 1D AFM spin chain model with zero toroidal moment.

A promising method for detecting ferrotoroidic order involves measuring the antisymmetric Compton profile [27–29] through Compton scattering experiments, an inelastic x-ray scattering technique [30]. Compton scattering refers to the phenomenon where the energy and momentum of photons change after colliding with electrons in matter. It is mainly used to study the electronic structure and magnetic properties of matter. The Compton profile reflects the distribution of electron momentum density, closely related to the symmetry of the crystal structure, electronic structure, and magnetic order. As a comparison, Raman scattering is also a scattering spectroscopy technique [31–33]. It is mainly used to study the structure and vibration modes of molecules by measuring the frequency changes of scattered light and is not usually used to directly measure magnetism.

The antisymmetric Compton profile is denoted as $J_A(p_z)=\frac{1}{2}[J(p_z)-J(-p_z)]$, where the Compton profile $J(p_z)=\frac{1}{n}\iint_{-\infty}^{\infty}\rho(\vec{p})dp_xdp_y$ is the projection of electron momentum density $\rho(\vec{p})$ along the specific direction (z) in momentum space. The electron momentum density $\rho(\vec{p})$ can be calculated from the wave function obtained through the first-principles calculations. For systems possessing either spatial-inversion symmetry or time-reversal symmetry, the Compton profile must satisfy $J(p_z)=J(-p_z)$. Consequently, the antisymmetric Compton profile is vanishing. However, in systems that simultaneously break spatial-inversion and time-reversal symmetries, such as the ferrotoroidic state, this symmetry

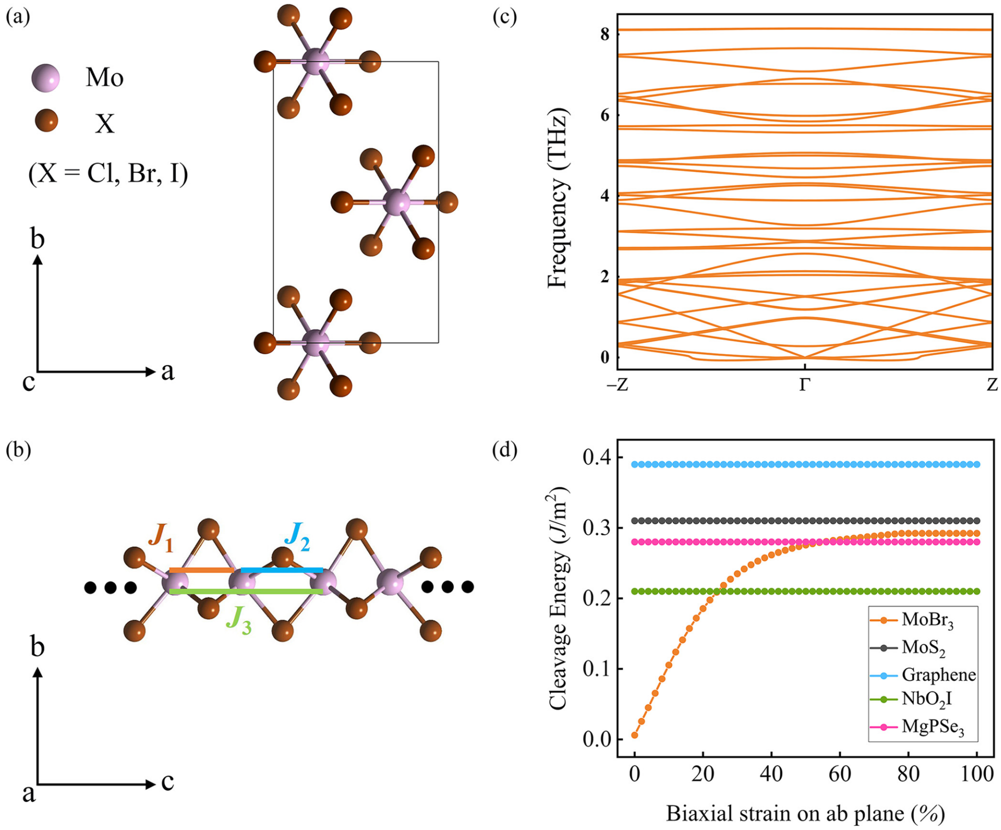

FIG. 2. (a) Crystal structure of bulk MoX_3. (b) The side view of 1D MoX_3 chain. The exchange interaction parameters between the short Mo-Mo pair, the long Mo-Mo pairs, and the next-nearest Mo-Mo pairs are denoted as J_1, J_2, and J_3, respectively. (c) The phonon spectrum of 1D MoBr$_3$. (d) The cleavage energy of MoBr$_3$.

constraint is no longer satisfied. This theoretical foundation enables the characterization of ferrotoroidic order using Compton profiles. According to the magnetoelectric (ME) multipole expansion theory [30], the antisymmetric Compton profile is related to the toroidal moment by $J_A(p_z) \simeq p_z \vec{t} \cdot \hat{z} \iint \frac{A^1(p)}{p} dp_x dp_y$, where $\vec{t}$ is the toroidal moment, p_z is the projection direction of the electron momentum, and $A^1(p)$ is the radial part of the multipole expansion. If a nonzero $\vec{t}$ exists in the system, such as t_z, then $J_A(p_z)$ will be nonzero and antisymmetric along the p_z direction. Therefore, the connection between the antisymmetric Compton profile and the ferrotoroidic moment provides an effective method for characterizing the ferrotoroidic order through the Compton scattering experiment.

Ferrotoroidic materials are exceedingly rare, and related research reports are limited. Currently, ferrotoroidic domains have been observed in LiCoPO$_4$ materials [34], where the manipulation of ferrotoroidic domains has been achieved under an external vortex electromagnetic field. Since two antiparallel spins constitute the simplest toroidal moment, we take 1D AFM spin chain as an example to illustrate the ferrotoroidicity. In a uniformly arranged 1D AFM spin chain in Fig. 1(a), no toroidal moment exists due to the space-inversion symmetry. However, the dimerized atomic structure and staggered AFM configuration break both the space-inversion symmetry and time-reversal symmetry, giving rise to a net toroidal moment in Fig. 1(b). By regulating the exchange interaction between adjacent sites, it is possible to obtain the different AFM order, as shown in Fig. 1(c). Due to the absence of a net toroidal moment, it can be classified as an antiferrotoroidic state. Consequently, Compton scattering serves as an alternative method for detecting and distinguishing the ferrotoroidic and antiferrotoroidic state. In this paper, we present findings on such a group of 1D van der Waals (vdW) ferrotoroidic materials. Due to the vdW interaction between 1D chains, the experimental realization of true 1D materials has been achieved [35]. Most importantly, we found that the hole doping can tune exchange interactions, leading to the transition from a ferrotoroidic state to an antiferrotoroidic state. This provides opportunities for controlling and detecting AFM order via Compton scattering. In the following, we take 1D MoX_3 as an example to to elaborate on our proposed concept.

B. Structures and stability of 1D MoX_3

The bulk MoBr$_3$ and MoI$_3$ have been experimentally synthesized [35–38]. Given the similarity of MoX_3, we will use MoBr$_3$ as a representative example to elucidate its structural, *Pnmm* electronic, and magnetic properties in detail. As shown in Fig. 2(a), bulk MoBr$_3$ adopts an orthorhombic structure with the space group *Pnmm*. The optimized lattice constants from first-principles calculations are $a = 5.545$ Å, $b = 11.330$ Å, and $c = 6.067$ Å, which closely align with experimental values. The bulk MoBr$_3$ consists of 1D chains by weak vdW interactions. Each 1D vdW chain in bulk MoBr$_3$

TABLE I. The lattice constant c along axis direction, d_s and d_l representing the distances between short Mo pairs and long Mo pairs, respectively. $r = d_s/d_l$ is the ratio of short to long Mo pairs. M is the magnetic moment and E_{gap} is the band gap of AFM$_1$ state.

System	c (Å)	d_s/d_l (Å)	r	M (μ_B)	E_{gap} (eV)
MoCl$_3$	5.839	2.663/3.175	0.84	1.900	1.427
MoBr$_3$	6.119	2.764/3.355	0.82	1.938	1.418
MoI$_3$	6.514	2.881/3.632	0.79	1.969	1.322

consists of an infinite series of face-sharing Mo-Br octahedral along the c axis. As illustrated in Fig. 2(b), these octahedra exhibit alternating short and long Mo–Mo bonds with lengths of 2.780 and 3.287 Å, respectively. The dimerization of Mo atoms in the 1D vdW chain distorts Mo-Br octahedra and breaks the spatial-inversion symmetry. The lattice constants of MoCl$_3$ and MoI$_3$ are also provided in Table I.

The optimized structure of 1D MoBr$_3$ chain exhibits slight deviations from its bulk counterpart. The lattice constant c increases to 6.119 Å, and the length of the long and short Mo–Mo bonds change to 3.354 and 2.764 Å, respectively, indicating a stronger dimerization due to the absence of interactions with surrounding chains. To assess the dynamic stability of the 1D MoBr$_3$ chain, we calculated the phonon spectrum with a 1 × 1 × 4 supercell. From the phonon spectrum as shown Fig. 2(c), we can find a small negative frequency (−0.06 THz) near the Γ point, which comes from collective vibration perpendicular to the 1D chain. It is particularly dependent on simulation parameters, such as supercell size and k-point sampling, which happens to be a common issue in *ab initio* calculations on low-dimensional materials. The similar situation also occurs in other reported 1D materials, WOI$_3$ [21] and VI$_3$ [39]. For these reasons, these negative frequencies are understood to be spurious. In addition, we also carried out *ab initio* molecular dynamics (MD) simulation at 300 K. We found that the structure is stable and there was no atomic diffusion phenomenon within 10 ps. Combined with our MD simulations and recent experimental reports on 1D single-chain MoI$_3$ [35], we think that 1D MoX_3 chains are stable.

The cleavage energy is calculated by gradually expanding lattice constants in the a- and b axes simultaneously by 2% at each step, as shown in Fig. 2(d), followed by structural optimization and total energy calculation. The calculated cleavage energy of MoBr$_3$ is approximately 0.29 J/m^2, comparable to that of other reported 2D materials such as CrI$_3$(0.31 J/m^2) [40], graphene (0.39 J/m^2) [40], NbO$_2$I (0.28 J/m^2) [41], and MgPSe$_3$(0.21 J/m^2) [42].

C. Magnetic ground state

Next, we focus on the magnetism of 1D vdW MoBr$_3$. Each Mo^{3+} ion is surrounded by six Br$^-$ ions. Therefore, the five degenerate 4d orbitals will split into three low-energy t_{2g} orbitals and two high-energy e_g orbitals under an octahedral crystal field. However, the distortion of the ideal octahedron due to dimerization leads to further minor splitting of the degenerate orbitals. The magnetism of MoBr$_3$ originates from the unpaired electrons in the d orbitals of Mo^{3+}(4d^3). The calculated local magnetic moment is about 1.9 μB/Mo [43]. To investigate the magnetic ground state of MoBr$_3$, we employed a 1 × 1 × 2 supercell to construct four different collinear magnetic configurations labeled FM, AFM$_1$, AFM$_2$, and AFM$_3$, as shown in Fig. 3. We use the Heisenberg model Hamiltonian [44] $H = \sum_{ij} J_{ij}\vec{S}_i \cdot \vec{S}_j$ to study magnetic exchange interaction, where J_{ij} is the isotropic exchange coefficient. The nearest-neighbor J_1 and J_2 correspond to the short and long Mo-Mo pairs respectively, and the next-nearest neighbor (NNN) exchange constant is defined as J_3, as shown in Fig. 2(b). By mapping four magnetic configurations to the Hamiltonian, we can obtain exchange constants listed in Table II. The positive values of J_1 and J_2 and the negative value of J_3 indicate that the AFM$_1$ magnetic configuration is the ground state of the 1D vdW MoBr$_3$ chain. Similarly, 1D MoCl$_3$ and MoI$_3$ also possess AFM$_1$ ground state.

TABLE II. The anisotropic and isotropic exchange constants, DM interaction coefficients, and the single-ion anisotropy coefficients for 1D MoBr$_3$.

Exchange constant	Isotropic case (meV/μ_B^2)	Anisotropic case (meV/μ_B^2)
J_1	18.001	14.853 (J_{1a})
		14.852 (J_{1b})
		15.089 (J_{1c})
J_2	3.206	2.626 (J_{2a})
		2.625 (J_{2b})
		2.701 (J_{2c})
J_3	−0.578	−0.578 (J_{3a})
		−0.578 (J_{3b})
		−0.564 (J_{3c})
DM interaction		meV/μ_B^2
$\vec{d}_1$		−0.113 (d_{1a})
		−0.113 (d_{1b})
		−0.114 (d_{1c})
$\vec{d}_2$		0.004 (d_{2a})
		0.004 (d_{2b})
		0.000 (d_{2c})
Single-ion anisotropy		meV/μ_B^2
D_a		−0.702
D_b		−0.702

According to the Mermin-Wanger theorem [45], long-range magnetic order is prohibited in low-dimensional (1D and 2D) materials in the absence of magnetic anisotropy. To understand the magnetic anisotropy in the 1D MoBr$_3$ chain, we define a spin Hamiltonian that includes the magnetic anisotropy and Dzyaloshinskii-Moriya (DM) interaction [46]:

$$H = \sum_{ij} \sum_{\alpha=(a,b,c)} J_{ij;\alpha}\vec{S}_i \cdot \vec{S}_j + \sum_{ij} \sum_{\alpha=(a,b,c)} \vec{d}_{ij;\alpha} \cdot (\vec{S}_i \times \vec{S}_j) + \sum_{i} \sum_{\alpha=(a,b)} D_{i;\alpha}(\vec{S}_i)^2, \tag{1}$$

where $J_{ij;\alpha}$ is the anisotropic exchange coefficient, $\vec{d}_{ij;\alpha}$ is the antisymmetric DM interaction vectors, $D_{i;\alpha}$ is the single-ion

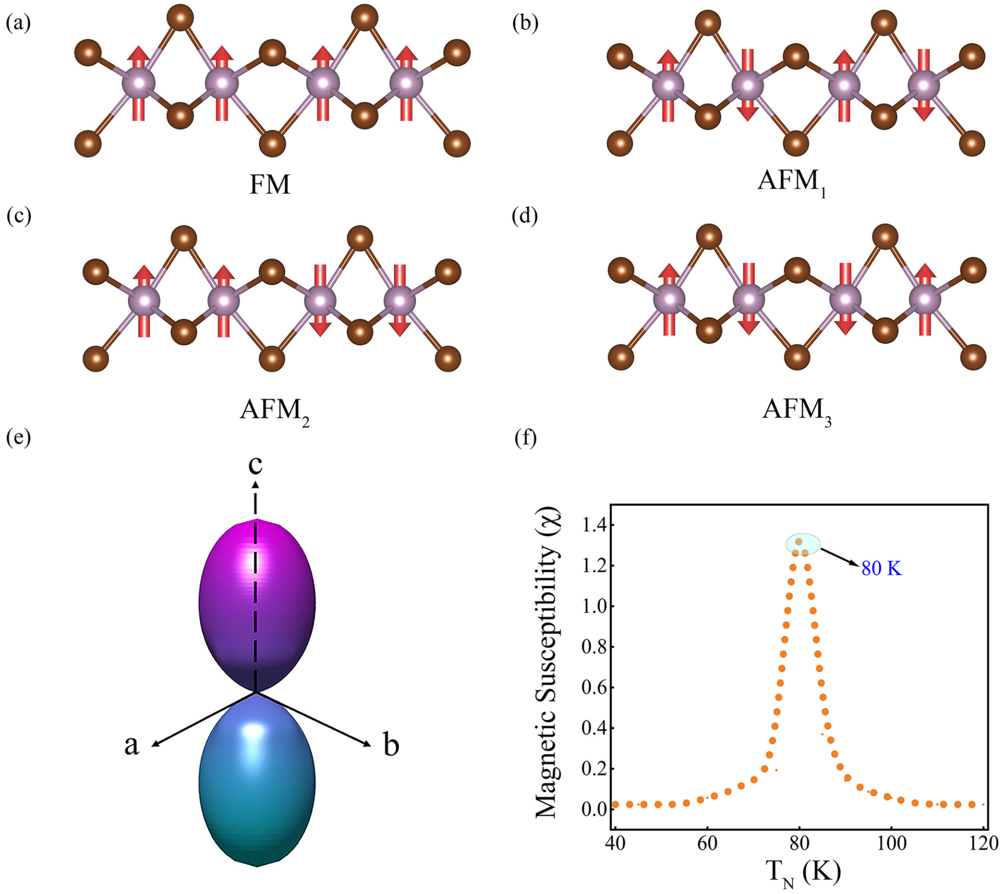

FIG. 3. (a)–(d) The four collinear magnetic configurations: FM, AFM$_1$, AFM$_2$, and AFM$_3$. (e) Isosurface of magnetic anisotropy energy of 1D MoBr$_3$ chain, where the *c* direction indicates the hard axis and the *ab* plane denotes the easy plane. (f) Temperature-dependent magnetic susceptibility, with a T_N of approximately 80 K.

anisotropy coefficient (with the *c* direction as reference), and $\vec{S}$ is the spin magnetic moment. Spin-orbit coupling (SOC) was considered in the calculation of magnetism anisotropy. To incorporate the DM interaction, we constructed four 90° noncollinear magnetic orders [47]. The DM interactions between the short Mo-Mo pairs and long Mo-Mo pairs are denoted as $\vec{d}_1$ and $\vec{d}_2$, respectively. All calculated coefficients are listed in Table II. Due to symmetry constraints, the DM interaction can be neglected. Our calculations indicate that $\vec{d}_1$ and $\vec{d}_2$ are much smaller than the exchange interaction coefficients, indicating that 1D MoBr$_3$ chain can preserve the AFM$_1$ magnetic state [48,49].

Although the formation of spin spirals can be neglected, the single-ion anisotropy remains strong compared to other materials. The calculated single-ion anisotropy coefficient is −0.702 meV/Mo, which is larger than that of 2D CrI$_3$ (−0.26 meV/Cr) [50]. To determine the MAE, we employed the torque method, varying the direction of magnetic moments uniformly throughout space as shown in Fig. 3(e). The results show that the *ab* plane is the easy plane and the hard axis is along the *c* direction. The energy difference between the easy plane and hard axis is 1.78 meV/Mo, which is larger than that of the 2D CrI$_3$ (0.65 meV/Cr) [44]. The larger MAE suggests the potential for achieving stable long-range magnetic order and collective excitation in the 1D MoBr$_3$ chain. Using the above effective spin Hamiltonian, we performed classical MC stimulations to estimate the T_N of the AFM order. The calculated T_N is about 80 K, as shown in Fig. 3(f). This T_N is comparable to those of known 1D magnetic semiconductors such as CrSbSe$_3$ (170 K) [17], VI$_3$ (80 K) [19], and CuBr$_3$ (35 K) [20].

In addition, we have also evaluated the interchain exchange interactions in bulk. We found that each 1D single chain in bulk still maintains the AFM$_1$ ground state. The interchain nearest-neighboring exchange interactions J'_1 and next-nearest neighboring exchange interaction J'_2 are 0.14 and 0.04 meV, respectively. Because J'_2 is much smaller than J'_1, J'_1 dominates the interchain AFM magnetic coupling in bulk MoBr$_3$ [47].

D. AFM phase transition by carrier doping

We subsequently investigated the magnetic ground state of 1D MoBr$_3$ chain under carrier doping. The relationship between doping and magnetic ground state can be seen in Fig. 4(a). The magnetic ground state transitions from the AFM$_1$ state to AFM$_3$ state when the hole concentration exceeds 9.8×10^{13} cm^{-2}. Although a significant magnetic phase transition occurs, the local magnetic moments of Mo in both the AFM$_1$ and AFM$_3$ states decrease linearly within a narrow

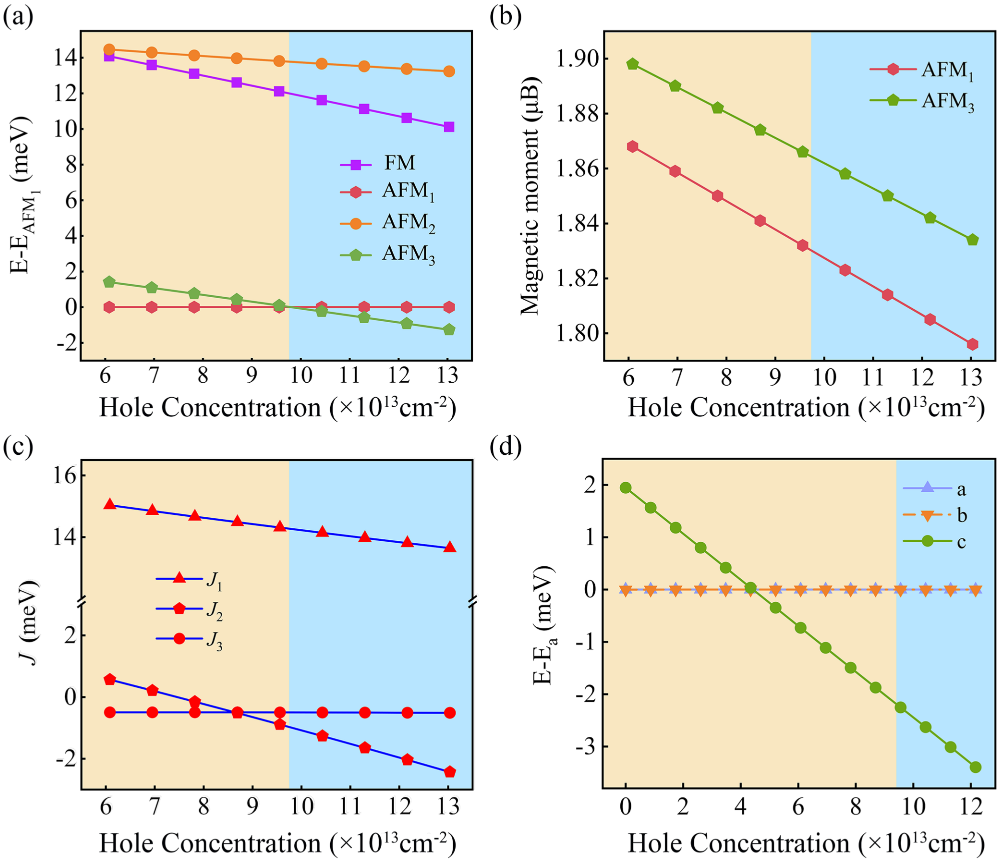

FIG. 4. (a) The energy difference between FM, AFM$_2$, and AFM$_3$ with AFM$_1$. The yellow region indicates the AFM$_1$ ground state and the blue region represents the AFM$_3$ ground state. (b) The magnetic moment of AFM$_1$ and AFM$_3$. (c) The exchange constants J_1, J_2, and J_3. (d) The change of MAE of AFM$_3$. All as functions of hole concentration.

range as the hole concentration increases by a fitted slope of 1 μ_B atom/hole, as shown in Fig. 4(b). This is because the valence-band top is entirely contributed by Mo-*d* orbitals, while the contribution of Br is far away from the valence-band top. So, removing electrons from half-occupied *d* orbitals corresponds to the reduction of spin magnetic moment on Mo. However, for materials with multiple orbital hybridization at the top of the valence band, the number of doped holes is not equivalent to a decrease in spin magnetic moment, e.g., CrI_3 under hole doping [51].

To elucidate the physical mechanism of magnetic phase transition, we studied the change of the exchange constants with hole concentration, as shown in Fig. 4(c). All three exchange constants decrease with increasing hole concentration. The strong exchange interaction J_1 between short Mo-Mo pairs remains consistently positive, indicating strong AFM coupling. The weaker J_2 will change from positive to negative when the hole concentration increases to 0.12 hole per Mo. We define the doping effective area as the periodic length of the single chain multiplied by the thickness of the atomic layer. So, doping concentration of 0.12 hole per Mo corresponds to 9.8×10^{13} cm^{-2}. It means the spin coupling between the long Mo-Mo pairs change from AFM to FM and thus the magnetic ground state becomes AFM$_3$. The NNN interaction J_3 is smallest and relatively insensitive to hole doping. Moreover, $MoCl_3$ and MoI_3 also undergo transitions from AFM$_1$ to AFM$_3$ at hole concentration of 1.5×10^{12} and 8.2×10^{13} cm^{-2}, respectively. Due to the requirement of spin conservation, the exchange interaction between half-occupied *d* orbitals tends towards AFM coupling, while FM coupling involves virtual transitions between occupied states and unoccupied states and thus is weaker compared to AFM coupling. So, in the absence of doping, the material is an AFM semiconductor with staggered AFM$_1$ ground states along the 1D axis direction. Due to the contribution of *d* orbitals at the top of the valence band, under hole doping the *d* orbitals will become partially occupied, which contributes additional FM exchange channels. With the increase of the hole doping concentration, FM exchange interaction begins to compete with AFM exchange interaction, manifested as a decrease of the exchange interaction coefficient and even a sign change. As shown in Fig. 4(c), although the exchange interaction coefficient J_1 decreases with increasing hole-doping concentration, it remains positive within the considered doping concentration range, indicating the maintenance of AFM coupling. The exchange interaction coefficient J_2 is much smaller than J_1. It decreases continuously with the increase of hole-doping concentration, and at a doping concentration of 0.12 hole per Mo, the sign changes from positive to negative, indicating a transition from AFM to FM coupling. Thus, the entire system transitions from AFM$_1$ state to AFM$_3$ state. The magnitude of the critical transition concentration depends on the specific material and

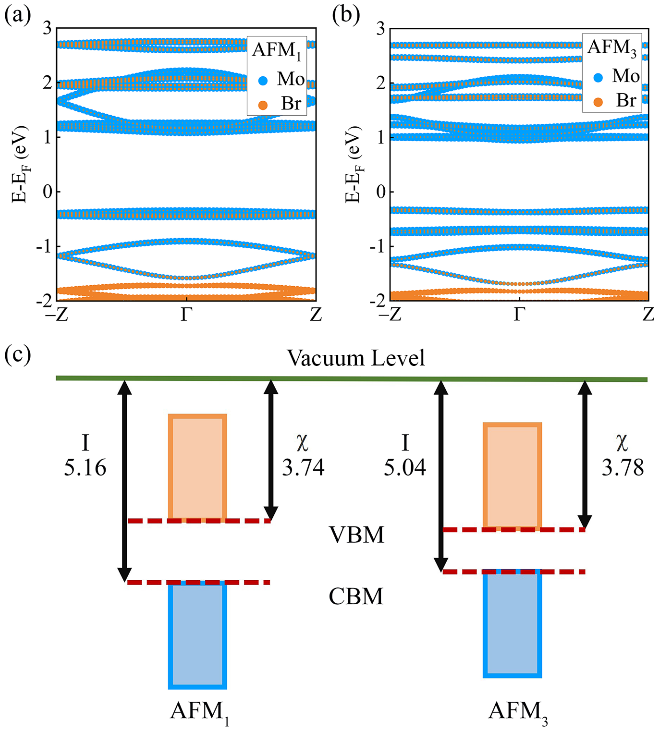

FIG. 5. (a), (b) Electronic band structures of 1D MoBr$_3$ in the AFM$_1$ and AFM$_3$ state, respectively. The blue and orange dots denote the Mo atoms and Br atoms, respectively. (c) Schematic illustration of band alignment for the AFM$_1$ and AFM$_3$ states.

electronic structures. So, the first-principles calculations are needed quantitatively to evaluate it. However, the underlying physical mechanisms and qualitative change trends can be theoretically predicted according to above physical picture. The mechanism of carrier doping-induced magnetic phase transitions has been also used in Ref. [21].

In addition, the magnetic phase transition under hole doping is also accompanied by a decrease in energy, which can be explained by the band alignment theory, as illustrated in Fig. 5. The band structures of 1D MoBr$_3$ with AFM$_1$ and AFM$_3$ magnetic states are shown in Figs. 5(a) and 5(b), respectively. Both AFM$_1$ and AFM$_3$ are semiconductors, with the valence-band maximum (VBM) and the conduction-band minimum (CBM) primarily composed of Mo orbitals. The ionization energy I is defined as the energy difference between the VBM and the vacuum energy level, and the electron affinity energy χ is the energy difference between the CBM and the vacuum energy level. I and χ determine the relative energy change of different phases under charge doping, as shown in Fig. 5(c). In the case of hole doping, electrons are removed from the VBM states. Since I of the AFM$_3$ phase is smaller that of the AFM$_1$ phase, the VBM of the AFM$_3$ phase is higher. Consequently, less energy is required to remove electrons from the AFM$_3$ phase compared to the AFM$_1$ phase, making the AFM$_3$ phase more energetically favorable under hole doping. A phase transition occurs when the doping concentration reaches a critical value of $9.8 \times 10^{13}\ \mathrm{cm}^{-2}$. These findings are in complete agreement with the results presented in Fig. 4.

Another interesting finding is the magnetic phase transition from easy-plane ab to easy-axis c with the hole concentrations exceeding $9.8 \times 10^{13}\ \mathrm{cm}^{-2}$. Further research indicates that the easy plane of AFM$_1$ does not change with hole doping, while AFM$_3$ changes from easy plane to easy axis. As shown in Fig. 4(d), the MAE increases with increasing hole concentration. The tunability of MAE through hole doping can be explained by perturbation theory analysis [52]. Given a pair of valence (v) eigenstate Ψ_v and conduction (c) eigenstate Ψ_c, their contribution to MAE is given by

$$\Delta E_{vc} = \frac{1}{\Delta_{vc}}\left(\left|H_{vc}^{\mathrm{SOC}}(\vec{x})\right|^2 - \left|H_{vc}^{\mathrm{SOC}}(\vec{z})\right|^2\right), \tag{2}$$

where $H_{vc}^{\mathrm{SOC}}(\vec{n}) = \langle \Psi_v | H^{\mathrm{SOC}}(\vec{n}) | \Psi_c \rangle$ is the SOC matrix element and $\Delta_{vc} = \varepsilon_v - \varepsilon_c$. $H^{\mathrm{SOC}}(\vec{n}) = \xi\, \vec{\sigma} \cdot \vec{L}$, where $\vec{\sigma} = (\sigma_x, \ \sigma_y, \ \sigma_z)$ are the 2×2 Pauli matrices, $\vec{L}$ is the orbital angular momentum operator, and ξ is the SOC strength. The sign of ΔE_{vc} is determined by the spin and magnetic quantum number of orbital characters [53]. The sum of ΔE_{vc} in Eq. (2) over all valence-conduction pairs determines the MAE and easy axis. The Mo d-orbital projected band structure of AFM$_3$ is shown in Figs. 6(a)–6(e). The highest valence bands (VB) are mostly contributed by $d_{xy}/d_{x^2-y^2}$. The electron hopping from VB $d_{xy}/d_{x^2-y^2}$ to conduction band (CB) d_{xz}/d_{yz} contributes to both parallel chain and perpendicular chain magnetization, while the hopping between d_{xy} and $d_{x^2-y^2}$ contributes only to perpendicular chain magnetization. Upon hole doping, d_{xy} and $d_{x^2-y^2}$ become unoccupied, reducing the stability of perpendicular chain magnetization. Hence, as the hole concentration increases, the AFM$_3$ state undergoes a transition from easy plane of ab to easy axis of c. The isosurface of MAE for AFM$_3$ state under a hole concentration $9.8 \times 10^{13}\ \mathrm{cm}^{-2}$ is shown in Fig. 6(f), where the c direction is the easy axis.

E. Detection of 1D ferrotoroidicity by Compton scattering

By carefully comparing two AFM states, we identify AFM$_1$ state as a unique 1D ferrotoroidic state with nonzero toroidal moment, as schematically shown in Fig. 1(b). Recently, 1D ferrotoroidic order has also been predicted experimentally for the quasi-1D material Ba$_6$Cr$_2$S$_{10}$ [54]. In contrast, the AFM$_3$ state is an antiferrotoroidic order with zero toroidal moment in Fig. 1(c). The dimerized atomic structure and staggered AFM configuration breaks both space-inversion symmetry and time-reversal symmetry, giving rise to the probability of ME multipole moments [26,55].

Symmetry analysis reveals that the 1D AFM$_1$ MoBr$_3$ belongs to C_{2v} point group with the irreducible representation (IR) B_2. The character table of C_{2v} and corresponding ME multipoles are listed in Table III [47]. The nonvanishing toroidal moments t_y and quadrupole moments q_{xz} in the Cartesian coordinate system are shown in Table III. For the AFM$_1$ ferrotoroidic state, $J_A(p_z)$ is nonzero and exhibits antisymmetry, such that $J_A(p_z) = -J_A(-p_z)$. Two-dimensional (2D) antisymmetric Compton profiles of AFM$_1$ ferrotoroidic state in plane $p_x - p_y$ are calculated and shown in Fig. 7(a). The pattern is antisymmetric along p_y and remains symmetric along p_x, which is consistent with the symmetry analysis.

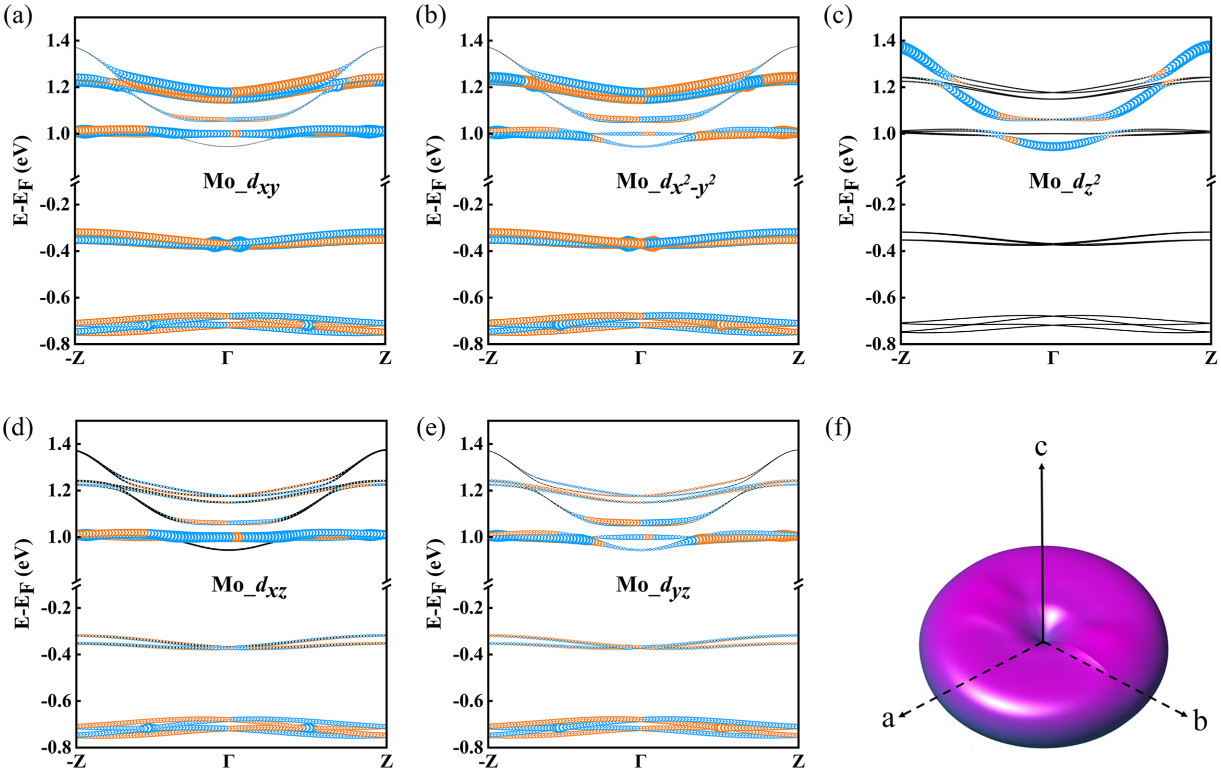

FIG. 6. (a)–(e) Mo-d orbital resolved electronic band structures of AFM$_3$. Yellow and blue color indicate spin-up and spin-down states, respectively. (f) Isosurface of MAE of AFM$_3$ under a hole concentration of 9.8×10^{13} cm^{-2}, where the c direction indicates the easy axis.

Meanwhile, the pattern also reveals the direction of the Néel vector, confirming the capability of Compton scattering to probe magnetic structures. For example, if the Néel vector is rotated 90° to align with the y direction, the toroidal moments t_x and quadrupole moments q_{yz} become nonzero, leading to the antisymmetric $J_A(p_x)$ along p_x, as shown in Fig. 7(b). In the AFM$_3$ configuration, no multipole moments are allowed. The calculated J_A is three orders of magnitude smaller than that of the AFM$_1$. Therefore, the antisymmetric Compton profile not only can effectively distinguish the ferrotoroidic AFM$_1$ and antiferrotoroidic AFM$_3$ state, but also can image the Néel vector switching, making it a valuable method for detecting AFM states.

III. CONCLUSION

In conclusion, we demonstrated a concept to control and detect the different AFM order in the 1D AFM spin chain through electrical and optical methods, and predicted a group of 1D materials MoX_3 ($X =$ Cl, Br, I) as examples. One-dimensional MoX_3 chain has alternating short and long Mo-Mo pairs along the periodic direction. The magnetic

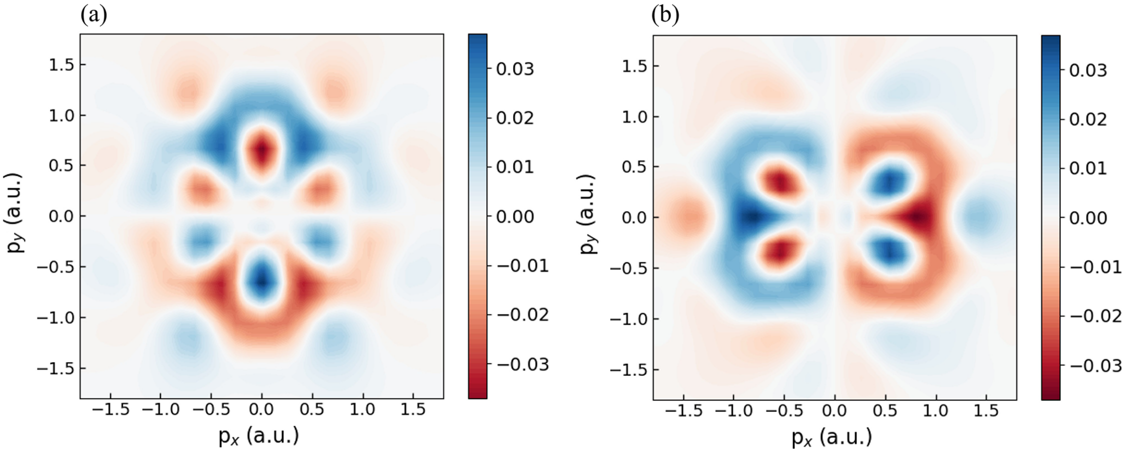

FIG. 7. Two-dimensional antisymmetric Compton profile in the $p_x - p_y$ plane corresponding to the AFM$_1$ state with the Néel vector along x- (a) or y (b) direction.

TABLE III. The basic functions for the ME multipoles with the C_{2v} point group. ME monopole (α), toroidal moment ($\vec{t}$), and quadrupole moment (q_{ij}).

IRs of C_{2v}	ME multioples	Basis in	
		Real space	***k*** space
A_1	t_z, q_{xy}	$(xm_y - ym_x)$, $(ym_x + xm_y)$	k_z
	α	$(xm_x + ym_y + zm_z)$	$k_x\,k_y\,k_z$
A_2	$q_{x^2-y^2}$	$(xm_x - ym_y)$	
	q_{z^2}	$(2zm_z - xm_x - ym_y)$	
B_1	t_x, q_{yz}	$(ym_z - zm_y)$, $(ym_z + zm_y)$	k_x
B_2	t_y, q_{xz}	$(zm_x - xm_z)$, $(zm_x + xm_z)$	k_y

ground state of MoX_3 is AFM with alternating opposite magnetic moments and the magnetic easy plane perpendicular to the periodic direction. The 1D dimerization structure and staggered AFM order indicates the existence of 1D ferrotoroidicity. Interestingly, as the hole concentration increases to $9.8 \times 10^{13}\ \mathrm{cm}^{-1}$, the ground state of 1D MoX_3 chain transitions from the ferrotoroidic AFM$_1$ to antiferrotoroidic AFM$_3$, accompanied by a sign change in the exchange interaction between the second-nearest neighboring Mo atoms. We revealed the physical mechanisms behind the magnetic phase transition and the change in the magnetic easy axis using band alignment theory and perturbation theory of SOC. Finally, we combined symmetry analysis and Compton scattering theory to illustrate how to distinguish between ferrotoroidic AFM$_1$ order and antiferrotoroidic AFM$_3$ order using antisymmetric Compton profiles. Therefore, the tunability and detectability of the magnetic order and ferrotoroidic order of 1D MoX_3 materials provides potential possibilities for future AFM spintronic applications.

IV. METHODS

A. DFT calculations

The calculations were performed based on density-functional theory (DFT) [56] using the projected augmented-wave method as implemented in the Vienna *Ab initio* Simulation Package (VASP) [57]. The general gradient approximation (GGA) [58] in the scheme of the Perdew-Burke-Ernzerhof (PBE) functional [59] was adopted to describe the exchange and correlation terms. The atomic positions were optimized with the maximum atomic force less than 0.001 eV/Å and the convergence of total energy was less than 1×10^{-6} eV. The DFT-D2 method of Grimme was used to account for van der Waals (vdW) interaction. The Brillouin zone was sampled with $1 \times 1 \times 15$ k points, and a large vacuum space of 25 Å was applied in the 1D MoX_3 to avoid the periodic interactions in the a- and b directions. The phonon spectra were calculated using the PHONOPY package [60] with a $1 \times 1 \times 4$ supercell. Spin-orbit coupling (SOC) was taken into account for computing the MAE and exchange coefficients in 1D MoX_3 chain. The MAEs were determined using the torque method [61,62]. Although a Hubbard U correction is typically not considered or only used with small U for Mo atoms [43,63], we investigated their impact on our main conclusions. Applying moderate effective U values ($U_{\mathrm{eff}} = U - J$) of 1 and 2 eV to Mo atoms revealed that our findings remained qualitatively unaffected [47]. Therefore, we present the results without U correction in the main text.

B. Monte Carlo simulations

The Néel temperature (T_{N}), a crucial parameter characterizing the antiferromagnetic phase transition, was determined using the classical Monte Carlo (MC) method [64,65] with the anisotropic Heisenberg XYZ model [66]. To ensure the detailed balance and to achieve the highest efficiency of program simulation for 1D MoX_3, the Hinzke-Nowak method [67] and the MC Metropolis algorithm [68] were used. At each temperature, the initial magnetic moments on the lattice points were completely randomized. The rationality of our results was confirmed by testing the effects of supercell size and simulation time per grid point. We employed a supercell of $1 \times 1 \times 200$ grids with a simulated temperature range of 0 to 150 K in 10 K increments. Magnetic susceptibility (χ) was chosen as the critical exponent due to the zero net magnetic moment of the AFM system.

C. Calculations of Compton profile

Compton profile is calculated by using ELK code [69] based on the linearized augmented plane-wave method. SOC was considered due to the asymmetric magnetization density rising from broken space-inversion symmetry and time-reversal symmetry. The GGA with PBE functional was used to describe the exchange and correlation terms. The electronic structure obtained from the ELK code agreed well with that from the VASP code. The Compton profile was presented in atomic units. We normalized the antisymmetric Compton profile by multiplying it by the vacuum thickness used in both the a- and b directions due to the 1D nature. This normalization ensures that the results are independent of the artificial vacuum layer.

ACKNOWLEDGEMENT

J.Q. acknowledges the support from the National Natural Science Foundation of China (Project No. 11974148). H.W. acknowledges the support provided by the Zhejiang Provincial Natural Science Foundation of China under Grant No. LDT23F04014F01, as well as the funding received from the National Natural Science Foundation of China (Project No. 12304049).

The authors declare no competing financial interest.

---

[1] S. Bhatti, R. Sbiaa, A. Hirohata, H. Ohno, S. Fukami, and S. N. Piramanayagam, Spintronics based random access memory: A review, Mater. Today **20**, 530 (2017).

[2] B. Dieny, I. L. Prejbeanu, K. Garello, P. Gambardella, P. Freitas, R. Lehndorff, W. Raberg, U. Ebels, S. O. Demokritov, J. Akerman, Opportunities and challenges for spintron-

ics in the microelectronics industry, Nat. Electron. **3**, 446 (2020).

[3] J. Han, R. Cheng, L. Liu, H. Ohno, and S. Fukami, Coherent antiferromagnetic spintronics, Nat. Mater. **22**, 684 (2023).

[4] T. Jungwirth, X. Marti, P. Wadley, and J. Wunderlich, Antiferromagnetic spintronics, Nat. Nanotechnol. **11**, 231 (2016).

[5] V. Baltz, A. Manchon, M. Tsoi, T. Moriyama, T. Ono, and Y. Tserkovnyak, Antiferromagnetic spintronics, Rev. Mod. Phys. **90**, 015005 (2018).

[6] D. Xiong, Y. Jiang, K. Shi, A. Du, Y. Yao *et al.*, Antiferromagnetic spintronics: An overview and outlook, Fundam. Res. **2**, 522 (2022).

[7] Y. Meng, W. Wang, and J. C. Ho, One-dimensional atomic chains for ultimate-scaled electronics, ACS Nano. **16**, 13314 (2022).

[8] Y. Zhang, L.-F. Lin, A. Moreo, and E. Dagotto, Electronic structure, dimer physics, orbital-selective behavior, and magnetic tendencies in the bilayer nickelate superconductor $La_3Ni_2O_7$ under pressure, Phys. Rev. B **108**, L180510 (2023).

[9] L.-F. Lin, Y. Zhang, A. Moreo, E. Dagotto, and S. Dong, Quasi-one-dimensional ferroelectricity and piezoelectricity in WOX_4 halogens, Phys. Rev. Mater. **3**, 111401(R) (2019).

[10] J. Gooth, B. Bradlyn, S. Honnali, C. Schindler, N. Kumar *et al.*, Axionic charge-density wave in the Weyl semimetal $(TaSe_4)_2I$, Nature. **575**, 315 (2019).

[11] Y. Zhang, L.-F. Lin, A. Moreo, and E. Dagotto, Electronic and magnetic properties of quasi-one-dimensional osmium halide $OsCl_4$, Appl. Phys. Lett. **120**, 023101 (2022).

[12] S. Lu, D. Guo, Z. Cheng, Y. Guo, C. Wang *et al.*, Controllable dimensionality conversion between 1D and 2D $CrCl_3$ magnetic nanostructures, Nat. Commun. **14**, 2465 (2023).

[13] R. Tuovinen, E. Perfetto, R. v. Leeuwen, G. Stefanucci, and M. A. Sentef, Distinguishing Majorana zero modes from impurity states through time-resolved transport, New J. Phys. **21**, 103038 (2019).

[14] H. Kim, A. Palacio-Morales, T. Posske, L. Rózsa, K. Palotás, L. Szunyogh, M. Thorwart, and R. Wiesendanger, Toward tailoring Majorana bound states in artificially constructed magnetic atom chains on elemental superconductors, Sci. Adv. **4**, 5251 (2018).

[15] S. Nadj-Perge, I. K. Drozdov, J. Li, H. Chen, S. Jeon, J. Seo, A. H. MacDonald, B. A. Bernevig, and A. Yazdani, Observation of Majorana fermions in ferromagnetic atomic chains on a superconductor, Science. **346**, 602 (2014).

[16] G. Wang, L. Liu, K. Yang, and H. Wu, $CrSbSe_3$: A pseudo one-dimensional ferromagnetic semiconductor, Phys. Rev. Mater. **5**, 124412 (2021).

[17] Y. Xun, Z. Zhu, X. Chen, and J. Qi, One-dimensional ferromagnetic semiconductor $CrSbSe_3$ with high Curie temperature and large magnetic anisotropy, Phys. Rev. B **104**, 085429 (2021).

[18] C. Su and L. He, Nanowires exfoliated from one-dimensional van der Waals transition metal trihalides and quadrihalides, Nanoscale Adv. **5**, 2096 (2023).

[19] S. Kumar, R. L. Kumawat, and B. Pathak, Spin-polarized current in ferromagnetic half-metallic transition-metal iodide nanowires, J. Phys. Chem. C **123**, 15717 (2019).

[20] S.-s. Li, Y.-p. Wang, S.-j. Hu, D. Chen, C.-w. Zhang, and S.-s. Yan, Robust half-metallicity in transition metal tribromide nanowires, Nanoscale. **10**, 15545 (2018).

[21] Z. Gong, Y. Xun, Z. Qian, K. Chang, J. Qi, and H. Wang, One-dimensional multiferroic semiconductor WOI_3: Unconventional anisotropic d^1 rule and bulk photovoltaic effect, Phys. Rev. B **110**, 094408 (2024).

[22] A. Urru, J.-R. Soh, N. Qureshi, A. Stunault, B. Roessli, H. M. Rønnow, and N. A. Spaldin, Neutron scattering from local magnetoelectric multipoles: A combined theoretical, computational, and experimental perspective, Phys. Rev. Res. **5**, 033147 (2023).

[23] C. G. Shull and J. S. Smart, Detection of antiferromagnetism by neutron diffraction, Phys. Rev. **76**, 1256 (1949).

[24] Z. Ni, A. V. Haglund, H. Wang, B. Xu, C. Bernhard *et al.*, Imaging the Néel vector switching in the monolayer antiferromagnet $MnPSe_3$ with strain-controlled Ising order, Nat. Nanotechnol. **16**, 782 (2021).

[25] M. Fiebig, D. Fröhlich, T. Lottermoser, V. V. Pavlov, R. V. Pisarev, and H. J. Weber, Second harmonic generation in the centrosymmetric antiferromagnet NiO, Phys. Rev. Lett. **87**, 137202 (2001).

[26] C. Ederer and N. A. Spaldin, Towards a microscopic theory of toroidal moments in bulk periodic crystals, Phys. Rev. B **76**, 214404 (2007).

[27] S. Bhowal and N. A. Spaldin, Revealing hidden magnetoelectric multipoles using Compton scattering, Phys. Rev. Res. **3**, 033185 (2021).

[28] A. Urru and N. A. Spaldin, Magnetic octupole tensor decomposition and second-order magnetoelectric effect, Ann. Phys. **447**, 168964 (2022).

[29] N. A. Spaldin, M. Fiebig, and M. Mostovoy, The toroidal moment in condensed-matter physics and its relation to the magnetoelectric effect, J. Phys.: Condens. Matter **20**, 434203 (2008).

[30] A. Sirindil, M. Quiquandon, and D. Gratias, Z-module defects in crystals, Acta Crystallogr. A. **73**, 427 (2017).

[31] P. M. Bergstrom and R. H. Pratt, An overview of the theories used in compton scattering calculations, Radiat. Phys. Chem. **50**, 3 (1997).

[32] J. Langer, D. Jimenez de Aberasturi, J. Aizpurua, R. A. Alvarez-Puebla, B. Auguié *et al.*, Present and future of surface-enhanced Raman scattering, ACS Nano **14**, 28 (2020).

[33] R. Pilot, R. Signorini, C. Durante, L. Orian, M. Bhamidipati, and L. Fabris, A review on surface-enhanced Raman scattering, Biosensors **9**, 57 (2019).

[34] B. B. Van Aken, J.-P. Rivera, H. Schmid, and M. Fiebig, Observation of ferrotoroidic domains, Nature (London). **449**, 702 (2007).

[35] J. Teeter, N. Y. Kim, T. Debnath, N. Sesing, T. Geremew *et al.*, Achieving the 1D atomic chain limit in Van der Waals crystals, Adv. Mater. **36**, 2409898 (2024).

[36] D. Babel, Die Verfeinerung der $MoBr_3$-struktur, J. Solid State Chem. **4**, 410 (1972).

[37] S. Merlino, L. Labella, F. Marchetti, and S. Toscani, Order–disorder transformation in $RuBr_3$ and $MoBr_3$: A two-dimensional Ising model, Chem. Mater. **16**, 3895 (2004).

[38] K. H. Choi, S. Oh, S. Chae, B. J. Jeong, B. J. Kim *et al.*, Low ligand field strength ion (I^-) mediated 1D inorganic material MoI_3: Synthesis and application to photo-detectors, J Alloy Compd. **853**, 157375 (2021).

[39] Z. Guo, Q. Chen, J. Yuan, K. Xia, X. Wang, and J. Sun, Ferromagnetic semiconducting VI_3 single-chain nanowire, J. Phys. Chem. C **124**, 2096 (2020).

[40] R. Zacharia, H. Ulbricht, and T. Hertel, Interlayer cohesive energy of graphite from thermal desorption of polyaromatic hydrocarbons, Phys. Rev. B **69**, 155406 (2004).

[41] H. Sun, K. Deng, E. Kan, and Y. Du, Second-order Jahn–Teller effect induced high-temperature ferroelectricity in two-dimensional NbO_2X ($X = I$, Br), Nanoscale Adv. **5**, 2979 (2023).

[42] C. Xu, H. Wang, Q. Min, Y. Xiong, S. Luo, and J. Yang, Electronic structure and optical property of 2D $MgPX_3$ ($X = S$ and Se) monolayer by density functional theory, Phys. Status Solidi B **261**, 2300448 (2024).

[43] C. Tan, X. Cao, X.-J. Wu, Q. He, J. Yang *et al.*, Recent advances in ultrathin two-dimensional nanomaterials, Chem. Rev. **117**, 6225 (2017).

[44] J. L. Lado and J. Fernández-Rossier, On the origin of magnetic anisotropy in two dimensional CrI_3, 2D Mater. **4**, 035002 (2017).

[45] N. D. Mermin and H. Wagner, Absence of ferromagnetism or antiferromagnetism in one- or two-dimensional isotropic Heisenberg models, Phys. Rev. Lett. **17**, 1133 (1966).

[46] M. Gong, Y. Qian, M. Yan, V. W. Scarola, and C. Zhang, Dzyaloshinskii-Moriya interaction and spiral order in spin-orbit coupled optical lattices, Sci. Rep. **5**, 10050 (2015).

[47] See Supplemental Material at http://link.aps.org/supplemental/10.1103/PhysRevB.111.134416 for more information about the character table of C_{2v} point group; the noncollinear magnetic configurations; the T_N and phonon spectrum of hole-doped $MoBr_3$; results with $U_{\mathrm{eff}} = 1$ and 2 eV and interchain exchange interaction in bulk.

[48] D.-L. Bao, A. O'Hara, S. Du, and S. T. Pantelides, Tunable, ferroelectricity-inducing, spin-spiral magnetic ordering in monolayer FeOCl, Nano Lett. **22**, 3598 (2022).

[49] J. H. Yang, Z. L. Li, X. Z. Lu, M. H. Whangbo, S.-H. Wei, X. G. Gong, and H. J. Xiang, Strong Dzyaloshinskii-Moriya interaction and origin of ferroelectricity in Cu_2OSeO_3, Phys. Rev. Lett. **109**, 107203 (2012).

[50] C. Xu, J. Feng, H. Xiang, and L. Bellaiche, Interplay between Kitaev interaction and single ion anisotropy in ferromagnetic CrI_3 and $CrGeTe_3$ monolayers, npj Comput. Mater. **4**, 57 (2018).

[51] S. Yu, Y. Wang, Y. Song, L. Xia, X. Yang, H. Fang, Q. Li, and X. Li, Hole doping induced half-metallic itinerant ferromagnetism and giant magnetoresistance in CrI_3 monolayer, Appl. Surf. Sci. **535**, 147693 (2021).

[52] G. H. O. Daalderop, P. J. Kelly, and M. F. H. Schuurmans, Magnetic anisotropy of a free-standing Co monolayer and of multilayers which contain Co monolayers, Phys. Rev. B **50**, 9989 (1994).

[53] H. Wang, J. Qi, and X. Qian, Electrically tunable high Curie temperature two-dimensional ferromagnetism in van der Waals layered crystals, Appl. Phys. Lett. **117**, 083102 (2020).

[54] J. Zhang, X. Wang, L. Zhou, G. Liu, D. T. Adroja *et al.*, A ferrotoroidic candidate with well-separated spin chains, Adv. Mater. **34**, 2106728 (2022).

[55] N. A. Spaldin, M. Fechner, E. Bousquet, A. Balatsky, and L. Nordström, Monopole-based formalism for the diagonal magnetoelectric response, Phys. Rev. B **88**, 094429 (2013).

[56] W. Kohn and L. J. Sham, Self-consistent equations including exchange and correlation effects, Phys. Rev. B **140**, A1133 (1965).

[57] G. Kresse and J. Furthmüller, Efficiency of ab-initio total energy calculations for metals and semiconductors using a plane-wave basis set, Comput. Mater. Sci. **6**, 15 (1996).

[58] S. Grimme, Semiempirical GGA-type density functional constructed with a long-range dispersion correction, J. Comput. Chem. **27**, 1787 (2006).

[59] J. P. Perdew, K. Burke, and M. Ernzerhof, Generalized gradient approximation made simple, Phys. Rev. Lett. **77**, 3865 (1996).

[60] A. Togo, First-principles phonon calculations with Phonopy and Phono3py, J. Phys. Soc. Jpn. **92**, 012001 (2022).

[61] X. Wang, R. Wu, D.-s. Wang, and A. J. Freeman, Torque method for the theoretical determination of magnetocrystalline anisotropy, Phys. Rev. B **54**, 61 (1996).

[62] R. Wu and A. J. Freeman, Spin–orbit induced magnetic phenomena in bulk metals and their surfaces and interfaces, J. Magn. Magn. Mater. **200**, 498 (1999).

[63] A. Mella, E. Suárez-Morell, and A. S. Nunez, Magnetic spirals and biquadratic exchange in 1D MoX_3 spin chains, J. Magn. Magn. Mater. **594**, 171882 (2024).

[64] J. Liu, Y. Qi, Z. Y. Meng, and L. Fu, Self-learning Monte Carlo method, Phys. Rev. B **95**, 041101(R) (2017).

[65] D. Hinzke and U. Nowak, Magnetization switching in a Heisenberg model for small ferromagnetic particles, Phys. Rev. B **58**, 265 (1998).

[66] C. Radhakrishnan, M. Parthasarathy, S. Jambulingam, and T. Byrnes, Quantum coherence of the Heisenberg spin models with Dzyaloshinsky-Moriya interactions, Sci. Rep. **7**, 13865 (2017).

[67] P. Asselin, R. F. L. Evans, J. Barker, R. W. Chantrell, R. Yanes, O. Chubykalo-Fesenko, D. Hinzke, and U. Nowak, Constrained Monte Carlo method and calculation of the temperature dependence of magnetic anisotropy, Phys. Rev. B **82**, 054415 (2010).

[68] P. Mathé and E. Novak, Simple Monte Carlo and the Metropolis algorithm, J. Complexity **23**, 673 (2007).

[69] The Elk Code, http://elk.sourceforge.net/.